J|A|C|S
ARTICLES

The Ru−Hbpp Water Oxidation Catalyst

Fernando Bozoglian,[†] Sophie Romain,[†] Mehmed Z. Ertem,[‡] Tanya K. Todorova,[§] Cristina Sens,[||] Joaquim Mola,[||] Montserrat Rodríguez,[||] Isabel Romero,[||] Jordi Benet-Buchholz,[†] Xavier Fontrodona,[||] Christopher J. Cramer,*[,‡] Laura Gagliardi,*[,‡,§] and Antoni Llobet*[,†,⊥]

Institute of Chemical Research of Catalonia (ICIQ), Avinguda Països Catalans 16, E-43007 Tarragona, Spain, Department of Chemistry, Department of Chemistry and Supercomputing Institute, University of Minnesota, 207 Pleasant Street SE, Minneapolis, Minnesota 55455, Department of Physical Chemistry, University of Geneva, 30 Quai Ernest Ansermet, CH-1211 Geneva, Switzerland, Serveis Tècnics de Recerca and Departament de Química, Universitat de Girona, E-17071 Girona, Spain, and Departament de Química, Universitat Autònoma de Barcelona, Cerdanyola del Vallès, E-08193 Barcelona, Spain

Received May 18, 2009; E-mail: cramer@umn.edu; gagliard@umn.edu; allobet@iciq.es

Abstract: A thorough characterization of the Ru−Hbpp (*in,in*-{[Ru^{II}(trpy)(H_2O)]$_2$(μ-bpp)}$^{3+}$ (trpy is 2,2′:6′,2″-terpyridine, bpp is bis(2-pyridyl)-3,5-pyrazolate)) water oxidation catalyst has been carried out employing structural (single crystal X-ray), spectroscopic (UV−vis and NMR), kinetic, and electrochemical (cyclic voltammetry) analyses. The latter reveals the existence of five different oxidation states generated by sequential oxidation of an initial II,II state to an ultimate, formal IV,IV oxidation state. Each of these oxidation states has been characterized by UV−vis spectroscopy, and their relative stabilities are reported. The electron transfer kinetics for individual one-electron oxidation steps have been measured by means of stopped flow techniques at temperatures ranging from 10 to 40 °C and associated second-order rate constants and activation parameters ($\Delta H^{\ddagger}$ and $\Delta S^{\ddagger}$) have been determined. Room-temperature rate constants for substitution of aqua ligands by MeCN as a function of oxidation state have been determined using UV−vis spectroscopy. Complete kinetic analysis has been carried out for the addition of 4 equiv of oxidant (Ce^{IV}) to the initial Ru−Hbpp catalyst in its II,II oxidation state. Subsequent to reaching the formal oxidation state IV,IV, an intermediate species is formed prior to oxygen evolution. Intermediate formation and oxygen evolution are both much slower than the preceding ET processes, and both are first order with regard to the catalyst; rate constants and activation parameters are reported for these steps. Theoretical modeling at density functional and multireference second-order perturbation theory levels provides a microscopic mechanism for key steps in intermediate formation and oxygen evolution that are consistent with experimental kinetic data and also oxygen labeling experiments, monitored *via* mass spectrometry (MS), that unambiguously establish that oxygen−oxygen bond formation proceeds intramolecularly. Finally, the Ru−Hbpp complex has also been studied under catalytic conditions as a function of time by means of manometric measurements and MS, and potential deactivation pathways are discussed.

1. Introduction

The oxidation of water to molecular oxygen is a reaction that takes place in the dark at the OEC-PSII.[1,2] It is a very interesting reaction to be modeled from a bioinorganic perspective so as to gain insight into the mechanism that operates in this natural system. It is of still greater importance from an energetic perspective, since water oxidation is the key bottleneck currently associated with the development of commercial light harvesting devices for the photoproduction of H_2 from water.[3] Water oxidation is a challenging task for a catalyst for two primary reasons: the first is the large endothermicity of the relevant reaction,

$$2H_2O \rightarrow O_2 + 4H^+ + 4e^- \qquad E^\circ = 1.23\ \text{V (vs. NHE) at pH} = 0 \quad (1)$$

and the second is the significant molecular complexity from a mechanistic point of view, since two protons and two electrons have to be removed from each of two water molecules and an oxygen−oxygen bond formed between them.

Beginning in 2008 there have been revolutionary developments with respect to the design of new transition metal complexes, characterized by different ligand sets and structures, that evolve molecular oxygen from water in the

[†] Institute of Chemical Research of Catalonia (ICIQ).
[‡] University of Minnesota.
[§] University of Geneva.
[||] Universitat de Girona.
[⊥] Universitat Autònoma de Barcelona.

(1) Yano, J.; Kern, J.; Sauer, K.; Latimer, M. J.; Pushkar, Y.; Biesiadka, J.; Loll, B.; Saenger, W.; Messinger, J.; Zouni, A.; Yachandra, V. K. *Science* **2006**, *314*, 821.
(2) Haumann, M.; Liebisch, P.; Müller, C.; Barra, M.; Grabolle, M.; Dau, H. *Science* **2005**, *310*, 1019.
(3) Balzani, V.; Credi, A.; Ventura, M. *ChemSusChem.* **2008**, *1*, 26.

Chart 1. The Ligands

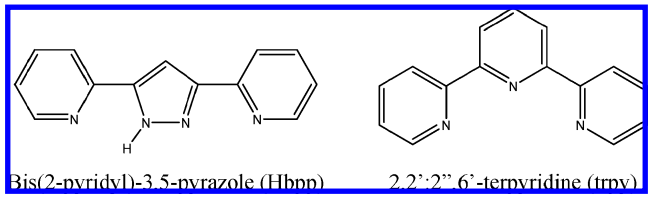

presence of an excess of a strong oxidant.[4] In most cases, however, the known compound is a precatalyst and the precise species responsible for catalytic activity is not well established. To engineer further improved catalysts, there is a substantial impetus to characterize fully the active species of existing complexes, including all relevant higher oxidation states, intermediates, and transition states, so as to establish the mechanism(s) by which they effect water oxidation.[5] For the elucidation of mechanistic details, theoretical modeling efforts can also be extremely helpful.

There are relatively few complexes characterized at a molecular level that have been shown to participate in the catalytic cycle of water oxidation to molecular oxygen. From a mechanistic standpoint there are three main types of Ru complexes that have been studied in some detail: (i) the so-called "blue dimer" *cis,cis*-$[Ru(bpy)_2(H_2O)]_2(\mu\text{-}O)^{4+}$ (bpy is 2,2′-bipyridine) where the dominant pathway leading to oxygen−oxygen bond formation is thought to involve nucleophilic attack of a solvent water molecule on a formal $Ru^V{=}O$ group;[6] (ii) two related mononuclear Ru complexes,[7] $[Ru(trpy)(b)(OH_2)]^{2+}$, (trpy is 2,2′:6′,2′-terpyridine; b is the bidentate ligand 2,2′-bipyrimidine or 2,2′-bipyrazine) which have been proposed to follow the same mechanism as in the blue dimer; and finally (iii) the binuclear[8] *in,in*-$\{[Ru^{II}(trpy)(H_2O)]_2(\mu\text{-bpp})\}^{3+}$ (Ru−Hbpp; trpy is 2,2′:6′,2″-terpyridine, bpp is bis(2-pyridyl)-3,5-pyrazolate) that, as we have reported in a recent communication, catalyzes O−O bond formation exclusively via an intramolecular pathway.[9]

In this work we provide a thorough spectroscopic, electrochemical, kinetic, and mechanistic characterization of the water oxidation catalyst $\{[Ru^{II}(trpy)(H_2O)]_2(\mu\text{-bpp})\}^{3+}$, $\mathbf{3}^{3+}$, containing the auxiliary ligands, trpy and bpp^- (See Chart 1 for drawings of the ligands). In addition, we present density functional theory (DFT) and multireference second-order perturbation theory (CASPT2) calculations for key microscopic steps in the catalytic cycle. This combination of experimental and theoretical data provides a complete, consistent, and comprehensive view of water oxidation complex $\mathbf{3}^{3+}$ and its related chemistry.

2. Results

2.1. Synthesis, Structure, and NMR Spectroscopy. The synthesis of catalyst $\mathbf{3}^{3+}$ begins with the reaction of $[RuCl_3trpy]$ and deprotonated bpp^- ligand, in the presence of NEt_3 (which acts as reducing agent), to generate the Cl-bridged dinuclear complex $\mathbf{1}^{2+}$.

$$2[Ru^{III}Cl_3trpy] + Bpp^- \xrightarrow{NEt_3} \underset{\mathbf{1}^{2+}}{\{[Ru^{II}(trpy)]_2(\mu\text{-}Cl)(\mu\text{-bpp})\}^{2+}} \quad (2)$$

The Cl bridging ligand is next replaced by a bridging acetato ligand in $\mathbf{2}^{2+}$ that can be transformed to the diaqua complex $\mathbf{3}^{3+}$ in aqueous acid.

$$\underset{\mathbf{1}^{2+}}{\{[Ru^{II}(trpy)]_2(\mu\text{-Cl})(\mu\text{-bpp})\}^{2+}} + OAc^- \xrightarrow{\text{Acetone-}H_2O} \underset{\mathbf{2}^{2+}}{\{[Ru^{II}(trpy)]_2(\mu\text{-bpp})(\mu\text{-OAc})\}^{2+}} + Cl^- \quad (3)$$

$$\underset{\mathbf{2}^{2+}}{\{[Ru^{II}(trpy)]_2(\mu\text{-bpp})(\mu\text{-OAc})\}^{2+}} + 2\,H_2O \xrightarrow{H^+} \underset{\mathbf{3}^{3+}}{\{[Ru^{II}(trpy)(H_2O)]_2(\mu\text{-bpp})\}^{3+}} + OAc^- \quad (4)$$

We hereafter abbreviate $\mathbf{3}^{3+}$ as "$H_2O{-}Ru^{II}Ru^{II}{-}OH_2$" since most of the chemistry that will be described here takes place at the Ru and aqua sites while the auxiliary trpy and bpp ligands remain unchanged. For the sake of brevity, we will not indicate overall charge in abbreviated formulas. Figure 1 displays the Ortep plots at 50% probability of the cationic site of $H_2O{-}Ru^{II}Ru^{II}{-}OH$ and of $\mathbf{2}^{2+}$ that cocrystallize (occupancy factor of 74% and 26%, respectively) in the same unit cell from a slow evaporation of $\mathbf{2}(PF_6)_2$ in an acetone/diethyl ether solution.

In the crystal structure it can be observed that the *in,in* disposition of the H_2O and OH^- ligands places the oxygen atoms in positions similar to those occupied by the oxygen atoms of the anionic AcO^- bridging ligand. Both complexes possess a pseudo-C_2 axis in the plane of the pyrazolate ring, probably due to packing interactions in the unit cell.

NMR analysis of $\mathbf{2}^{2+}$ added to a solution of 0.1 M deuterated triflic acid in D_2O indicates free acetate and the bis-aqua complex $H_2O{-}Ru^{II}Ru^{II}{-}OH_2$ to be the only species present at significant concentrations. The latter exhibits C_{2v} symmetry, suggesting that there is a fast exchange process that interconverts the enantiomeric forms associated with aqua positions above and below the plane of the pyrazolate moiety. The activation barrier for this interconversion is estimated to be lower than 19.2 kJ/mol based on VT-NMR analysis. DOSY (Diffusion Ordered NMR Spectroscopy) experiments in d_6-acetone/H_2O 0.1 M CF_3SO_3D (4/1) shown in Figure 2, indicate that the volume of $\mathbf{3}^{3+}$ is roughly 1.5 times that of $Ru(trpy)_2{}^{2+}$, and thus clearly indicates the nonexistence of aggregates through potential hydrogen bonding involving the $Ru{-}OH_2$ groups.

Slow evaporation of $\mathbf{3}^{3+}$ in a 0.1 M triflic acid solution leads to the formation of crystals of $\mathbf{4}^{2+}$. The single-crystal X-ray

(4) Sala, X.; Rodriguez, M.; Romero, I.; Escriche, L.; Llobet, A. *Angew. Chem., Int. Ed.* **2009**, *48*, 2842.
(5) Betley, T. A.; Wu, Q.; Van Voorhis, T.; Nocera, D. G. *Inorg. Chem.* **2008**, *47*, 1849.
(6) (a) Binstead, R. A.; Chronister, C. W.; Ni, J.; Hartshorn, C. M.; Meyer, T. J. *J. Am. Chem. Soc.* **2000**, *122*, 8464. (b) Yamada, H.; Siems, W. F.; Koike, T.; Hurst, J. *J. Am. Chem. Soc.* **2004**, *126*, 9786. (c) Liu, F.; Concepcion, J. J.; Jurss, J. W.; Cardolaccia, T.; Templeton, J. L.; Meyer, T. J. *Inorg. Chem.* **2008**, *47*, 1727. (d) Concepcion, J. J.; Jurss, J. W.; Templeton, J. L.; Meyer, T. J. *Proc. Nat. Acad. Sci. U.S.A.* **2008**, *105*, 17635.
(7) Concepcion, J. J.; Jurss, J. W.; Templeton, J. L.; Meyer, T. J. *J. Am. Chem. Soc.* **2008**, *130*, 16462.
(8) (a) Sens, C.; Romero, I.; Rodríguez, M.; Llobet, A.; Parella, T.; Benet-Buchholz, J. *J. Am. Chem. Soc.* **2004**, *126*, 7798. (b) Mola, J.; Mas-Marza, E.; Sala, X.; Romero, I.; Rodriguez, M.; Vinas, C.; Parella, T.; Llobet, A. *Angew. Chem., Int. Ed.* **2008**, *47*, 5830.
(9) Romain, S.; Bozoglian, F.; Sala, X.; Llobet, A. *J. Am. Chem. Soc.* **2009**, *131*, 2768.

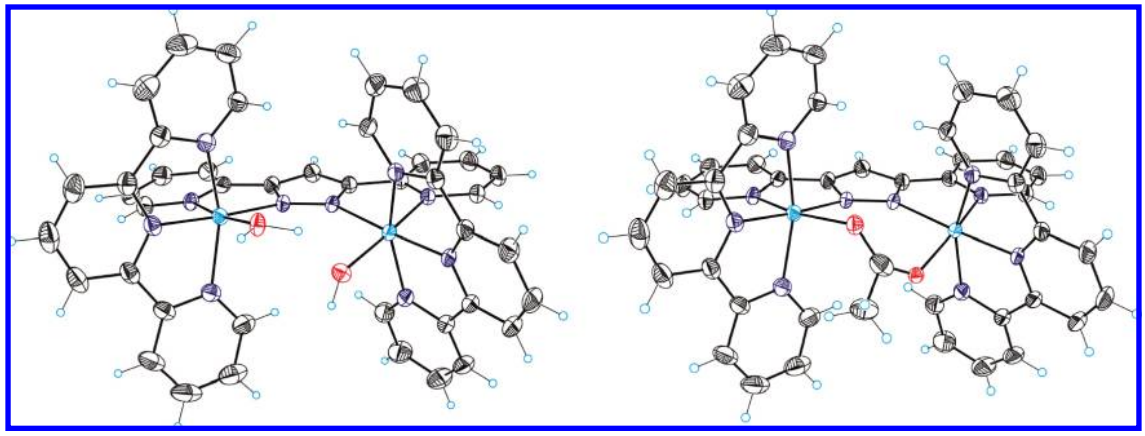

Figure 1. Ortep plots at 50% probability for the cationic part of complexes $H_2O-Ru^{II}Ru^{II}-OH$ (left) and $\mathbf{2}^{2+}$ (right) found with 74% and 26% occupancy, respectively. Selected interatomic distances for $H_2O-Ru^{II}Ru^{II}-OH$ in Å: Ru···Ru, 4.50; O···O, 2.47. Color codes: Ru, cyan; N, blue; O, red; C, gray; H, light blue.

structure for $\mathbf{4}^{2+}$ has a triflate anion bridging the two Ru centers (see Supporting Information),

$$\underset{\mathbf{3}^{3+}}{\{[Ru^{II}(trpy)(H_2O)]_2(\mu\text{-bpp})\}^{3+}} + CF_3SO_3^- \rightleftharpoons \underset{\mathbf{4}^{2+}}{\{[Ru^{II}(trpy)]_2(\mu\text{-bpp})(\mu\text{-}CF_3SO_3)\}^{2+}} + 2\,H_2O \quad (5)$$

This observation together with the NMR data indicates that the equilibrium shown in eq 5 is highly favored toward the left but that crystals of $\mathbf{4}^{2+}$ could be isolated because of their evidently very low solubility.

2.2. Redox Properties and UV−Visible Spectroscopy. Redox properties have been investigated by means of cyclic voltammetric and Coulombimetric experiments. Figure 3 presents the cyclic voltammogram of a saturated solution of the $H_2O-Ru^{II}Ru^{II}-OH_2$ complex at pH = 1.0 in a 0.1 M triflic acid solution and its Pourbaix diagram.

Three chemically reversible and electrochemically quasireversible redox processes are observed that can be assigned to the following reactions,

$$H_2O-Ru^{III}Ru^{II}-OH_2 + 1\,e^- \rightarrow H_2O-Ru^{II}Ru^{II}-OH_2 \qquad E_{1/2} = 0.59\ V\ (\Delta E = 64\ mV) \quad (6)$$

$$HO-Ru^{III}Ru^{III}-OH_2 + 1\,e^- + 1H^+ \rightarrow H_2O-Ru^{III}Ru^{II}-OH_2 \qquad E_{1/2} = 0.65\ V\ (\Delta E = 64\ mV) \quad (7)$$

$$HO-Ru^{IV}Ru^{III}-OH + 1\,e^- + 1H^+ \rightarrow HO-Ru^{III}Ru^{III}-OH_2 \qquad E_{1/2} = 0.88\ V\ (\Delta E = 110\ mV) \quad (8)$$

A fourth chemically irreversible wave of very weak intensity is also observed that can be tentatively assigned to

$$O-Ru^{IV}Ru^{IV}-O + 1\,e^- + 2H^+ \rightarrow HO-Ru^{IV}Ru^{III}-OH \qquad E_a \approx 1.10\ V \quad (9)$$

The proton content of the different species has been deduced from the corresponding Pourbaix diagram that is also presented in Figure 3, and that has been built up from cyclic voltammetric experiments at different pH. The proton assignment has been carried out according to precedent information obtained for these types of complexes, but we cannot distinguish between $HO-Ru^{IV}Ru^{III}-OH$ and $O-Ru^{IV}Ru^{III}-OH_2$. We note that, in sharp contrast to the blue dimer,[10] at pH = 1.0 all of the redox processes we observe are one-electron in character. The only

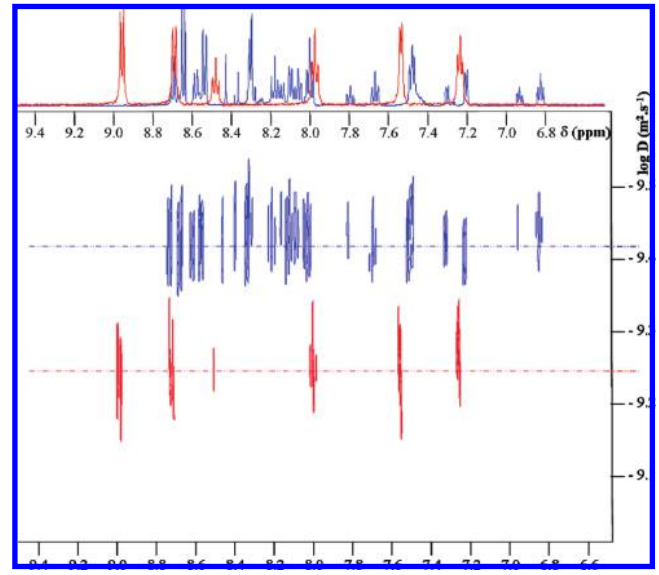

Figure 2. ^1H NMR DOSY spectra of 3.5 mM solutions of $\mathbf{3}^{3+}$ (blue) and $Ru(trpy)_2^{2+}$ (red) in d_6-acetone/H_2O 0.1 M CF_3SO_3D (4/1).

two-electron process we observe, which is in the range of pH = 5.5−8.5, is

$$HO-Ru^{IV}Ru^{III}-OH + 2e^- + H^+ \rightarrow HO-Ru^{III}Ru^{II}-OH_2 \qquad E_a = 0.5\ V\ \text{at pH} = 7.0 \quad (10)$$

Figure 4 shows UV−vis spectra of the diaqua complex $H_2O-Ru^{II}Ru^{II}-OH_2$ at pH = 1.0 and those generated by the $1e^-$ sequential oxidation of this species, namely $H_2O-Ru^{III}-Ru^{II}-OH_2$, $HO-Ru^{III}Ru^{III}-OH_2$, and $HO-Ru^{IV}Ru^{III}-OH$ at the same pH.

UV−vis spectroscopy has also been used to monitor acid−base titration at oxidation state II,II,

$$H_2O-Ru^{II}Ru^{II}-OH_2 \rightarrow H_2O-Ru^{II}Ru^{II}-OH + H^+ \qquad pK_a = 6.8 \quad (11)$$

and the obtained pK_a value is in very good agreement with that extracted from the Pourbaix diagram based on the slope change for the $E^{o'}$(III,II/II,II) redox potential. The UV−vis of the $H_2O-Ru^{II}Ru^{II}-OH_2$ educt is typical for Ru(II)-aqua polypyridyl types of complexes,[11] exhibiting an MLCT transition in the

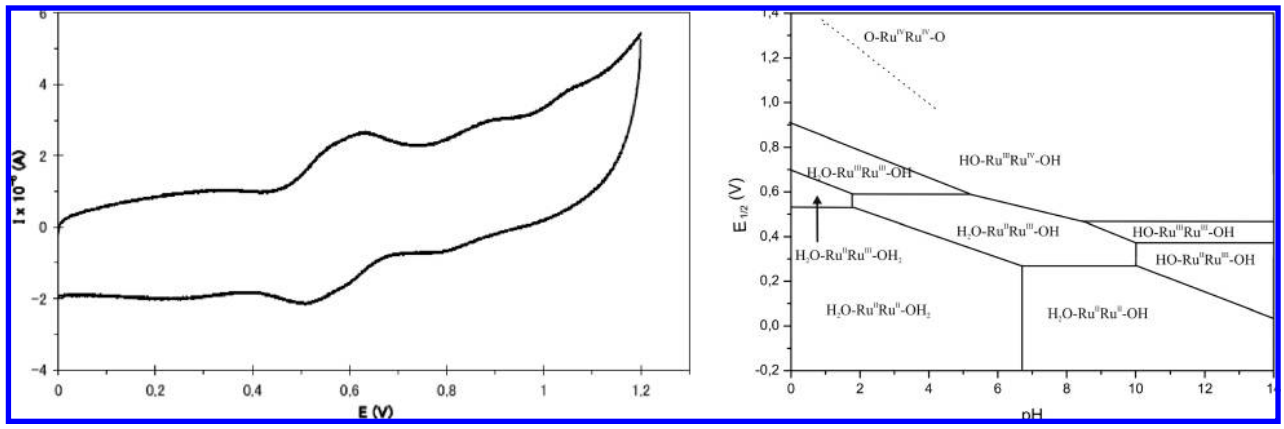

Figure 3. Left, cyclic voltammetry of $\mathbf{3}^{3+}$ at pH = 1.0 in 0.1 M triflic acid aqueous solution, carried out at ν = 100 mV/s with a glassy carbon working electrode (3 mm in diameter) using an SSCE reference electrode. Right, Pourbaix diagram for $\mathbf{3}^{3+}$ obtained from cyclic voltammetric experiments. The represented IV,IV/IV,III redox potential has been obtained from DFT calculations.[16]

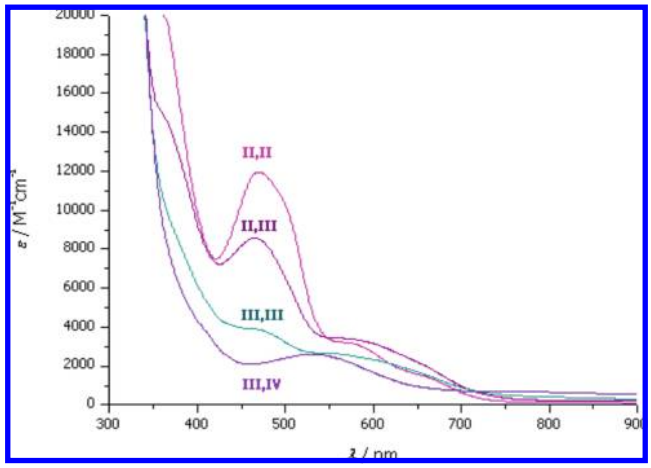

Figure 4. UV−vis spectroscopy for $H_2O-Ru^{II}Ru^{II}-OH_2$ ($\mathbf{3}^{3+}$) and three consecutively one-electron oxidized products at pH = 1.0 in a 0.1 M triflic acid solution. Roman numerals indicate formal oxidation states of the metal centers.

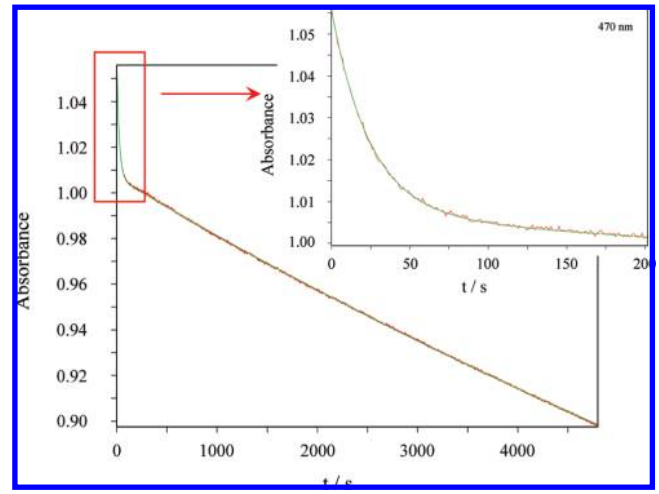

Figure 5. Plot of absorption vs time (one point per second) at λ_{max} = 470 nm (red) and fit (green) for an 88.0 μM solution of $\mathbf{3}^{3+}$and MeCN 0.70 mM at 25.0 °C. The inset shows an enlargement of the first 200 s of the substitution reaction.

region of 350−550 nm, very weak d−d transitions at longer wavelengths, and ligand-based (trpy, bpp) $\pi-\pi^*$ transition in the 250−350 nm range. Increasing the oxidation state produces mainly a decrease of the intensity of the bands in the 350−550 nm range, and for the III,IV oxidation state this zone is basically featureless. Under acidic conditions (pH = 1 triflic acid) at 25 °C the oxidation states II,II and II,III are quite stable in solution while oxidation state III,III is stable for only about 1 h and oxidation state III,IV is stable for only about 10 min. Once oxidation state IV,IV is reached, it immediately begins to evolve molecular oxygen, and thus its spectrum has been determined by singular value decomposition analysis using Specfit, *vide infra*.

2.3. Substitution Kinetics and Oxidation State. Initially we tried to measure the substitution kinetics of the labile aqua ligands as a function of oxidation state by NMR using water labeled with ^{17}O. However these experiments were unsuccessful owing to the low solubility of the $H_2O-Ru^{II}Ru^{II}-OH_2$ complex. We were successful, however, in measuring the substitution kinetics of the aqua ligands by MeCN in 0.1 M triflic acid solutions, according to the following equations,

$$H_2O-Ru^{II}Ru^{II}-OH_2 + MeCN \xrightarrow{k_{s1}} H_2O-Ru^{II}Ru^{II}-MeCN + H_2O \quad (12)$$

$$H_2O-Ru^{II}Ru^{II}-MeCN + MeCN \xrightarrow{k_{s2}} MeCN-Ru^{II}Ru^{II}-MeCN + H_2O \quad (13)$$

Kinetics were monitored by UV−vis spectroscopy as shown in Figure 5 and Supporting Information for the two consecutive substitutions indicated in eqs 12 and 13.

(10) Gestern, S. W.; Samuels, G. J.; Meyer, T. J. *J. Am. Chem. Soc.* **1982**, *104*, 4029.

(11) (a) Rodríguez, M.; Romero, I.; Llobet, A.; Deronzier, A.; Biner, M.; Parella, T.; Stoeckli-Evans, H. *Inorg. Chem.* **2001**, *40*, 4150. (b) Barkawi, K.; Llobet, A.; Meyer, T. J. *J. Am. Chem. Soc.* **1988**, *110*, 7751. (c) Llobet, A. *Inorg. Chim. Acta* **1994**, *221*, 125. (d) Laurent, F.; Plantalech, P.; Donnadieu, B.; Jiménez, A.; Hernández, F.; Martínez-Ripoll, M.; Biner, M.; Llobet, A. *Polyhedron* **1999**, *18*, 3321. (e) Romero, I.; Rodríguez, M.; Llobet, A.; Collomb-Dunand-Sauthier, M.-N.; Deronzier, A.; Parella, T.; Soteckli-Evans, H. *J. Chem. Soc., Dalton Trans.* **2000**, 1689. (f) Sala, X.; Romero, I.; Rodríguez, M.; Llobet, A.; González, G.; Martínez, M.; Benet-Buchholz, J. *Inorg. Chem.* **2004**, *43*, 5403. (g) Sala, X.; Plantalech, E.; Poater, A.; Rodríguez, M.; Romero, I.; Solà, M.; Llobet, A.; Jansat, S.; Gómez, M.; Stoeckli-Evans, H.; Benet-Buchholz, J. *Chem.—Eur. J.* **2006**, *12*, 2798.

Table 1. Rate Constants and $t_{1/2}$ for the First and Second Substitution Processes for Different Oxidation States Measured at pH =1.0 with Triflic Acid under Pseudo-first-order Conditions ([MeCN]/[Ru−Hbpp]) = 3.24×10^2), T = 25.0 °C

	first MeCN substitution		second MeCN substitution	
complex	k_1 (s^{-1})	$t_{1/2}$ (s)	k_2 (s^{-1})	$t_{1/2}$ (s)
$H_2O-Ru^{II}Ru^{II}-OH_2$	$4.0.10^{-2}$	1.70×10	$5.8.10^{-5}$	1.19×10^4
$H_2O-Ru^{III}Ru^{II}-OH_2$	$8.8\ 10^{-4}$	7.80×10^2		
$H_2O-Ru^{III}Ru^{III}-OH$	$2.0.10^{-5}$	3.45×10^4		

Assuming pseudo-first-order behavior (under pseudo-first-order conditions ([MeCN]/[Ru−Hbpp]) = 3.24×10^2), for the two substitutions we calculate the corresponding rate constants presented in Table 1 as determined from Specfit.[12]

As can be observed in Table 1, substitution takes place very quickly for oxidation state II,II, with a half-life of 17 s. For the second substitution, the rate decreases by more than 2 orders of magnitude, showing a $t_{1/2}$ of 3.3 h. This significant slowing can be assigned to two factors: electronic coupling between the two Ru centers through the pyrazolate bridge and the increase in steric demand associated with the initially coordinated MeCN ligand. For the first substitution reaction, as the oxidation state of the $H_2O-Ru^{II}Ru^{II}-OH_2$ complex is increased, there is a dramatic decrease of the rate constant, consistent with related Ru polypyridylic complexes previously reported in the literature.[13] These results for the first substitution reaction are of interest since under comparable steric constraints the rate decrease must exclusively be due to electronic coupling between the metal centers.

The implications of these results for the Ru−aqua exchange kinetics are important. In particular, to extract useful mechanistic data, it is imperative to have a different degree of oxygen labeling in the catalyst and in the water solvent. As deduced from the MeCN results, this should be feasible if the $H_2O-Ru^{II}Ru^{II}-OH_2$ catalyst is first oxidized to oxidation state III,III and then the solvent is diluted with a different proportion of labeled water.

2.4. Electron Transfer Kinetics and Intermediate Species. Kinetic studies on the stepwise oxidation of $H_2O-Ru^{II}Ru^{II}-OH_2$ to $HO-Ru^{III}Ru^{IV}-OH$ were conducted with stoichiometric or less than stoichiometric amounts of added Ce^{IV} and monitored by UV−vis spectroscopy at pH = 1.0 (see Figure 6). Rates were investigated at various concentrations of the Ru catalyst but always with $[Ce^{IV}] < [H_2O-Ru^{II}Ru^{II}-OH_2]$ to avoid complications from reaching higher than $n + 1$ oxidation states.

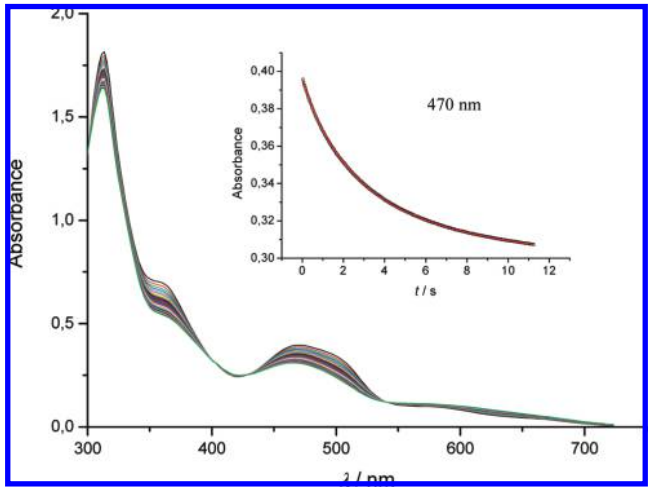

Figure 6. Spectral changes with time in aqueous 0.1 M triflic acid when a 3.4×10^{-5} M solution of $H_2O-Ru^{II}Ru^{II}-H_2O$ is mixed with the same volume of a 3.0×10^{-5} M solution of Ce^{IV}. Inset, changes in absorbance vs time at 470 nm and the fit. The black points correspond to the experimental data and the red trace to the fit.

$$H_2O-Ru^{II}Ru^{II}-OH_2 + Ce^{IV} \xrightarrow{k_{ET1}} H_2O-Ru^{III}Ru^{II}-OH_2 + Ce^{III} \quad (14)$$

$$H_2O-Ru^{III}Ru^{II}-OH_2 + Ce^{IV} \xrightarrow{k_{ET2}} HO-Ru^{III}Ru^{III}-OH_2 + Ce^{III} + H^+ \quad (15)$$

$$HO-Ru^{III}Ru^{III}-OH_2 + Ce^{IV} \xrightarrow{k_{ET3}} HO-Ru^{IV}Ru^{III}-OH + Ce^{III} + H^+ \quad (16)$$

The rate laws are first order in Ce^{IV} and first order in Ru complex for all of the oxidation steps, and the values obtained are presented in Table 2 and in the Supporting Information. At 10 °C, the values of k_{ET} decrease with increasing oxidation state. For the oxidation of the III,IV to IV,IV species, the kinetics were studied under pseudo-first-order conditions (in all cases $[Ce^{IV}]$ was at least 10 times that of III,IV) since this is the slowest ET step and because the evolution of the IV,IV species to the intermediate is much slower than the antecedent ET steps. The dependence of k_{obs} with $[Ce^{IV}]$ is graphically shown in the Supporting Information. The nonlinear behavior observed is interpreted in terms of a significant value of K_{OS} for an outer-sphere mechanism (the values of K_{OS} in the temperature range measured span $(2-5) \times 10^2\ M^{-1}$) that is indicative of important nonelectrostatic interactions, probably hydrogen bonds, in the generation of the outer-sphere complex prior to the electron transfer. An alternative mechanism may involve the Ce^{IV} addition across a ruthenyl terminal oxo atom as has been proposed for the blue dimer case.[14]

$$HO-Ru^{IV}Ru^{III}-OH + Ce^{IV} \xrightarrow{k_{ET4}} O-Ru^{IV}Ru^{IV}-O + Ce^{III} + 2H^+ \quad (17)$$

The temperature dependence of k_{ET} was also measured in the range 10−40 °C permitting determination of activation parameters from Eyring plots (Supporting Information); these are also reported in Table 2. Upon addition of the fourth equivalent of Ce^{IV}, a series of kinetic events leads to the formation of molecular oxygen. Since the system is catalytic, addition of more than 4 equiv of Ce^{IV} repeats the catalytic cycle. To isolate the previously mentioned kinetic events, the experiments at this point were performed with a 1:4 ratio of $H_2O-Ru^{II}Ru^{II}-OH_2$:Ce^{IV}. As in the previous cases, the reactions were monitored by UV−vis spectroscopy and were carried out within the temperature range of 10 °C (from now on considered as low T) to 40 °C (high T) as shown in Figure 7.

At low temperatures the kinetic model that best fits the data is consistent with three consecutive first order reactions A → B → C → D. On the basis of singular value decomposition (SVD) analysis performed by Specfit, we assign A as oxidation state III,IV, B as IV,IV, C as an intermediate "I" that is formed prior to oxygen evolution, and D as a product in a lower oxidation state generated concomitant with the release of molecular oxygen. These processes are graphically represented in Scheme 1. The labels A−D used here are based on the number of kinetic processes obtained from Sepcfit and are assigned to complex species based on their kinetic and spectroscopic properties.

Thus at low T the kinetic analysis can be summarized with the following equations:

$$H_2O{-}Ru^{II}Ru^{II}{-}OH_2 + 3Ce^{IV} \xrightarrow{\text{very fast}} HO{-}Ru^{III}Ru^{IV}{-}OH + 3Ce^{III} + 2H^+ \quad (18)$$

$$HO{-}Ru^{III}Ru^{IV}{-}OH + Ce^{IV} \xrightarrow{k_{ET4(A\rightarrow B)}} O{-}Ru^{IV}Ru^{IV}{-}O + Ce^{III} \quad (19)$$

$$O{-}Ru^{IV}Ru^{IV}{-}O \xrightarrow{k_{I(B\rightarrow C)}} I \quad (20)$$

$$I \xrightarrow{k_{O2(C\rightarrow D)}} (Ru^{II}Ru^{II}) + O2 \quad (21)$$

A similar analysis was carried out at higher T and the kinetic model that fits the data is now consistent with four consecutive first order reactions A → B → C → D → E (the labels here denote the processes obtained by Specfit and, as in the previous case, are assigned to complex species on the basis of their spectrosocopic and kinetic properties). Under these conditions the III,IV oxidation state is not observed and the first species detected after the addition of 4 equiv of Ce^{IV} is the IV,IV oxidation state. Thus in this particular case the reactions observed are the following:

$$H_2O{-}Ru^{II}Ru^{II}{-}OH_2 + 4Ce^{IV} \xrightarrow{\text{very fast}} O{-}Ru^{IV}Ru^{IV}{-}O + 4Ce^{III} + 4H^+ \quad (22)$$

$$O{-}Ru^{IV}Ru^{IV}{-}O \xrightarrow{k_{I(A\rightarrow B)}} I \quad (23)$$

$$I \xrightarrow{k_{O2(B\rightarrow C)}} (Ru^{II}Ru^{II}) + O_2 \quad (24)$$

$$(Ru^{II}Ru^{II}) \xrightarrow{(C\rightarrow D)} (Ru^{II}Ru^{II})' \quad (25)$$

$$(Ru^{II}Ru^{II})' \xrightarrow{(D\rightarrow E)} (Ru^{II}Ru^{II})'' \quad (26)$$

At higher temperatures, with 4 equiv of Ce^{IV} and allowing the system to progress for a sufficiently long time, we observe the evolution of the $(Ru^{II}Ru^{II})$ species to two newly reduced species that could have different degrees and/or modes of anion coordination and that are indicated in eqs 25 and 26 as $(Ru^{II}Ru^{II})'$ and $(Ru^{II}Ru^{II})''$. In the presence of excess Ce^{IV}, these species will be competing with the catalytic cycle that evolves molecular oxygen. Importantly, in the range 10−40 °C the kinetics are fully consistent with a single kinetic model, namely, that indicated at the start of this section.

2.5. Stoichiometric Oxygen Generation. To gain further insight into the nature of the catalytic process, oxygen evolution experiments were carried out with ^{18}O-labeled catalyst and solvent. A different degree of labeled catalyst and solvent was achieved by initial oxidation of the $H_2O{-}Ru^{II}Ru^{II}{-}OH_2$ catalyst from oxidation state II,II to III,III, followed by dilution with either labeled or nonlabeled water. This strategy is viable because with oxidation state III,III the aqua substitution kinetics are very slow, as described above. The experiments were also designed so that only one turnover could take place, and the gases formed were analyzed on line via mass spectrometry (MS). Table 3 lists the results of the labeling experiments with a different degree of labeled catalyst and solvent whose profiles are depicted in Figure 8 and in the Supporting Information.

Scheme 1. Reaction Scheme that Generates Oxygen upon Addition of Ce^{IV} to $H_2O{-}Ru^{II}Ru^{II}{-}OH_2$

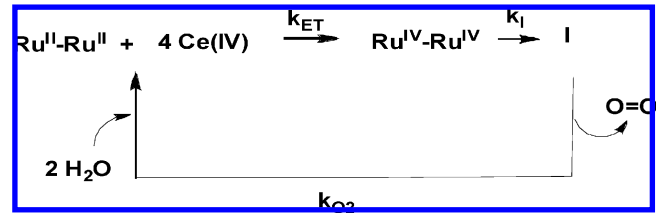

For comparison purposes, Table 3 indicates the values assuming two alternative reaction mechanisms and also the values that would be obtained assuming fast aqua exchange before oxygen formation. The two mechanisms considered are intramolecular O−O bond formation (Intra, Path 2) and H_2O nucleophilic attack (Nuc, Path 1)[15,16] (Figure 9, right and left side, respectively). The labeling experiments unambiguously demonstrate that the only mechanism operating in this case is the intramolecular one.

2.6. DFT and CASPT2 Calculations. Calculations were carried out in order to gain further insight into the relative energetics of alternative reaction pathways and potential intermediates associated with the oxygen−oxygen bond formation promoted by the Ru−Hbpp water oxidation catalyst. In particular, we characterized stationary points along different reaction paths at the M06-L level of density functional theory and then assessed the reliability of various aspects of the DFT calculations by comparing them to the multireference correlated wave function theory CASPT2. For simplicity, all energies described below are from M06-L calculations unless otherwise specified, but we found the two theories to make very similar predictions for state energy splittings in individual complexes (both predicting the same ground states in every case) and also agreeing reasonably well on relative energies for reaction paths along which the relevant CAS active space did not change from reactants to products. Such agreement between the two theories, M06-L and CASPT2, leads to increased confidence in their quantitative utilities given their complementary natures.

We note that the M06-L functional has been specifically recommended for transition-metal containing systems,[17] and benchmark studies have confirmed its excellent accuracy in this respect.[18] As we will compare specifically to prior work

(12) Specfit is a trademark of Spectrum Software Associates.
(13) (a) Allen, L. R.; Craft, P. P.; Durham, B.; Walsh, J. *Inorg. Chem.* **1987**, *23*, 53. (b) Reddy, K. B.; Cho, M. P.; Wishart, J. F.; Emge, T. J.; Isied, S. S. *Inorg. Chem.* **1996**, *35*, 7241. (c) Sullivan, B. P.; Conrad, D.; Meyer, T. J. *Inorg. Chem.* **1985**, *24*, 3640. (d) Isied, S. S.; Taube, H. *Inorg. Chem.* **1976**, *15*, 3070. (e) Isied, S. S.; Taube, H. *Inorg. Chem.* **1974**, *13*, 1545–1551. (f) Franco, D. W.; Taube, H. *Inorg. Chem.* **1978**, *17*, 571–578. (g) Rappaport, I.; Helm, L.; Merbach, A. E.; Bernhard, P.; Ludi, A. *Inorg. Chem.* **1988**, *27*, 873. (h) Yamada, H.; Koike, T.; Hurst, J. K. *J. Am. Chem. Soc.* **2001**, *123*, 12775.
(14) Yamada, H.; Hurst, J. K. *J. Am. Chem. Soc.* **2000**, *122*, 5303.
(15) Romero, I.; Rodriguez, M.; Sens, C.; Mola, J.; Kollipara, M. R.; Francas, L.; Mas-Marza, E.; Escriche, L.; Llobet, A. *Inorg. Chem.* **2008**, *47*, 1824.
(16) Yang, X.; Baik, M.-H. *J. Am. Chem. Soc.* **2008**, *130*, 16231.
(17) Zhao, Y.; Truhlar, D. G. *J. Chem. Phys.* **2006**, *125*, 194101.
(18) (a) Zheng, J. J.; Zhao, Y.; Truhlar, D. G. *J. Chem. Theory Comput.* **2007**, *3*, 569–582. (b) Torker, S.; Merki, D.; Chen, P. *J. Am. Chem. Soc.* **2008**, *130*, 4808–4814. (c) Zhao, Y.; Truhlar, D. G. *Acc. Chem. Res.* **2008**, *41*, 157–167. (d) Zhao, Y.; Truhlar, D. G. *Theor. Chem. Acc.* **2008**, *120*, 215–241. (e) Cramer, C. J.; Gour, J. R.; Kinal, A.; Włoch, M.; Piecuch, P.; Moughal Shahi, A. R.; Gagliardi, L. *J. Phys. Chem. A* **2008**, *112*, 3754–3767. (f) Zhao, Y.; Truhlar, D. G. *J. Chem. Theory Comput.* **2009**, *5*, 324–333. (g) Korth, M.; Grimme, S. *J. Chem. Theory Comput.* **2009**, *5*, 993–1003.

Table 2. Rate Constants Calculated at 10.0 °C, Together with Their Corresponding Activation Parameters, for the Reaction of the $H_2O-Ru^{II}Ru^{II}-OH_2$ (**3**$^{3+}$) Catalyst and Ce^{IV} in 0.1 M CF_3SO_3H

	K	process	*k* values	$\Delta H^{\ddagger}$ (kJ mol^{-1})	$\Delta S^{\ddagger}$ (J mol^{-1} K^{-1})
k_{ETn} M^{-1} s^{-1}	k_{ET1}	$H_2O-Ru^{II}Ru^{II}-OH_2 \rightarrow H_2O-Ru^{III}Ru^{II}-OH_2$	$(5.0 \pm 0.3) \times 10^4$	22 ± 1	-84 ± 3
	k_{ET2}	$H_2O-Ru^{III}Ru^{II}-OH_2 \rightarrow HO-Ru^{III}Ru^{III}-OH_2$	$(3.9 \pm 0.1) \times 10^4$	34 ± 2	-45 ± 7
	k_{ET3}	$HO-Ru^{III}Ru^{III}-OH_2 \rightarrow HO-Ru^{IV}Ru^{III}-OH$	$(3.2 \pm 0.2) \times 10^4$	29 ± 2	-65 ± 5
	k_{ET4}	$HO-Ru^{IV}Ru^{III}-OH \rightarrow O-Ru^{IV}Ru^{IV}-O$	$(5.0 \pm 0.8) \times 10^2$	23 ± 3	-122 ± 10
k s^{-1}	k_1	$O-Ru^{IV}Ru^{IV}-O \rightarrow I$	$(6.1 \pm 0.3) \times 10^{-4}$	53 ± 3	-137 ± 9
	k_{O2}	$I \rightarrow Ru^{II}Ru^{II}$	$(1.4 \pm 0.1) \times 10^{-4}$	85 ± 8	-39 ± 27

employing the B3LYP functional below, we note that Zhao and Truhlar[17] and Torker et al.[18b] have found ligand binding energies in Ru-based Grubbs catalysts to be underestimated by B3LYP with average errors on the order of 46 kJ/mol compared to 4 kJ/mol for M06-L. Similarly, Cramer et al. observed B3LYP to poorly predict $LCuO_2$ relative isomer energies and state-energy splittings for a series of ligands L where M06-L offered the best agreement of several tested functionals compared to large multireference calculations and completely renormalized coupled cluster calculations.[18e] Even in organic-based systems, benchmark studies have indicated that M06-L provides improved estimates of thermochemistry and barrier heights compared to B3LYP by 5−20 kJ/mol.[18a,c,d,g]

The two reaction paths we examined begin from the common reactant $O-Ru^{IV}Ru^{IV}-O$ labeled **a** in Figure 9. We will address in future work the detailed electronic structures of the various intermediates and transition state (TS) structures appearing in Figure 9; here we restrict our theoretical discussion to those features, primarily energetic, that are most germane to a mechanistic understanding of the observed catalytic water oxidation. Reaction path 1 involves nucleophilic attack of a water molecule on one of the oxo fragments in **a**, which is best described as supporting two $Ru^{III}O^{\bullet -}$ units each one of which is triplet coupled across its Ru−O bond and the pair of which are weakly coupled in a quintet ground state (the range from quintet to singlet is predicted to be on the order of only 4 kJ/mol; a preference for Ru^{III} with a noninnocent oxidized ligand has also been noted recently by Roy et al. who reported that oxidation in dinuclear Ru^{III} phenoxides takes place at relatively low redox potentials to generate phenoxyl radicals rather than Ru^{IV} oxides[19]). While the nucleophilic attack is assisted by hydrogen bonding and ultimately proton transfer from the water molecule to the other oxo fragment, the predicted free energy of activation leading to TS structure **b** is predicted to be 134.3 kJ/mol in the gas phase and 143.9 kJ/mol in aqueous solution (accounting for bulk solvation effects using the SMD aqueous

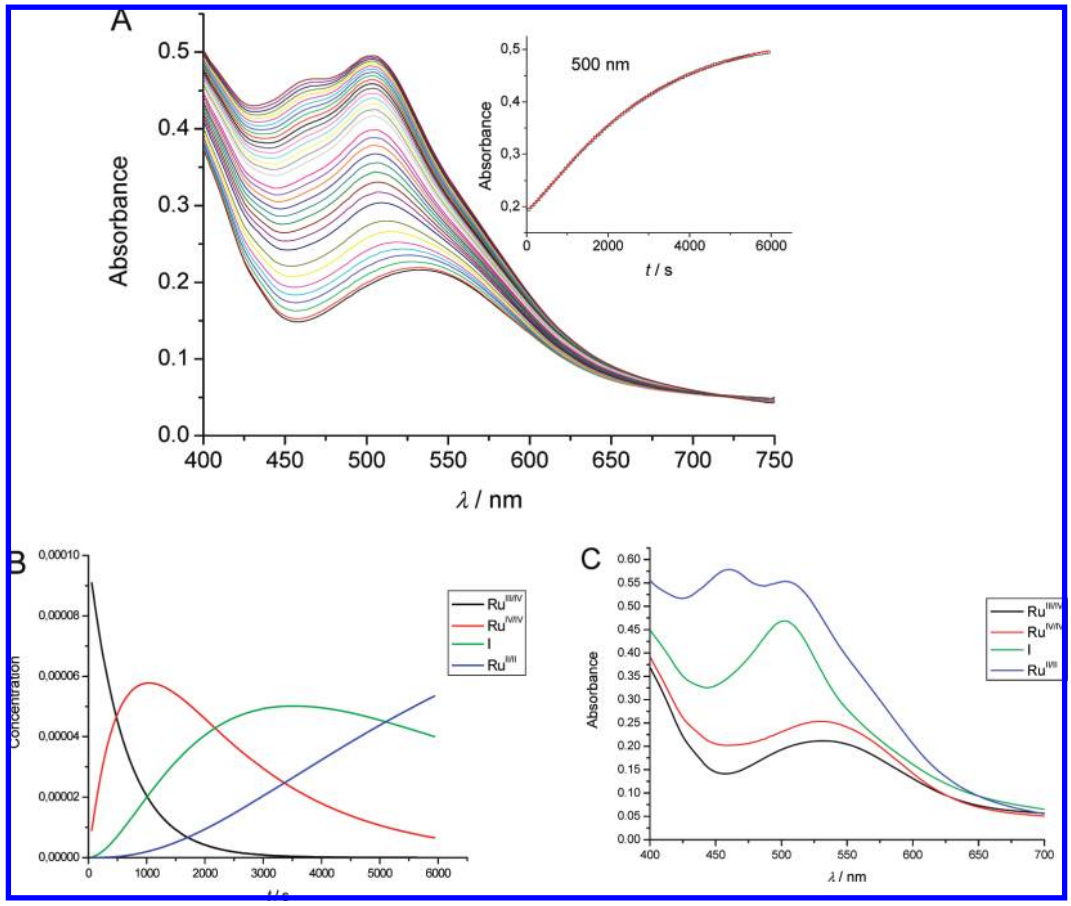

Figure 7. (A) Spectral changes vs time at 10.0 °C after addition of 4 equiv of Ce^{IV} to a 1.6×10^{-4} M solution of $H_2O-Ru^{II}Ru^{II}-H_2O$ in 0.1 M CF_3SO_3H. The inset shows the fit at $\lambda = 500$ nm. The black points correspond to the experimental data and the red trace to the fit. (B) Species distribution diagram. (C) Calculated spectra. Color code: blue, $Ru^{II,II}$ is $H_2O-Ru^{II}Ru^{II}-H_2O$; green, I is the intermediate; red, $Ru^{IV,IV}$ is $O-Ru^{IV}Ru^{IV}-O$; black, $Ru^{IV,III}$ is $HO-Ru^{IV}Ru^{III}-OH$.

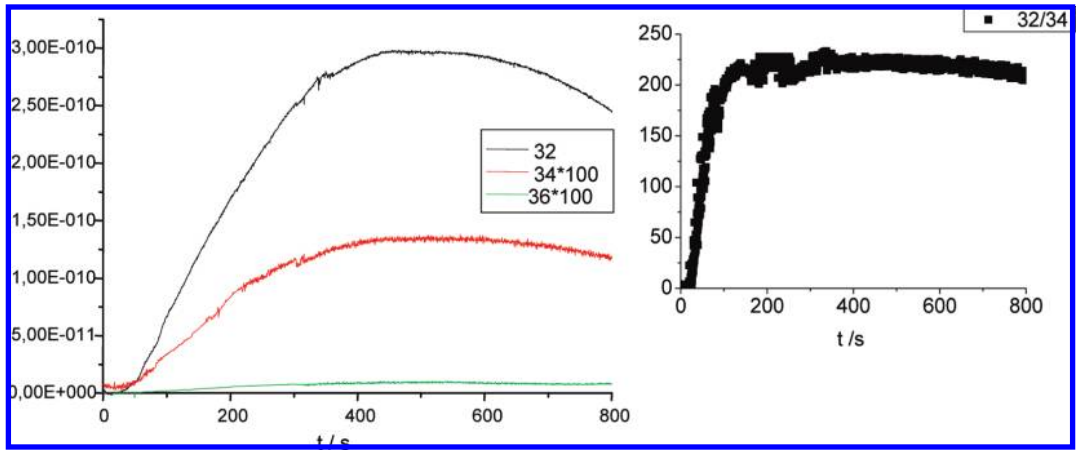

Figure 8. Left, mass spectra obtained in the case of > entries 1−3 described in Table 3 of the main text. The *y* axis units are "Intensity (cps)". Right, relative $^{32}O_2/^{34}O_2$ intensity as a function of time. The final concentration of the Ru complex is 3.0 mM, after the sequential addition of 2 and 5 equiv of Ce(IV).

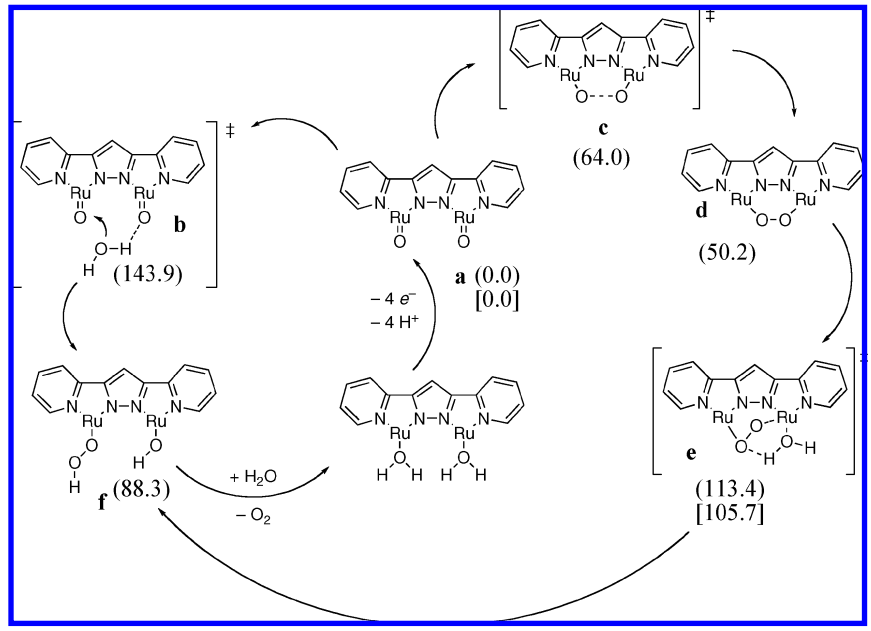

Figure 9. Reaction paths 1 (left) and 2 (right) for oxygen generation from O−$Ru^{IV}Ru^{IV}$−O (labeled **a** in this Figure). Terpyridine ligands on Ru atoms are not shown for clarity. Free energies (kJ/mol) in aqueous solution relative to **a** + H_2O are provided for structures **b**, **c** + H_2O, **d** + H_2O, **e**, and **f** as values in parentheses. The values in brackets for structures **a** and **e** indicate relative energies including an additional explicit molecule of H_2O in the first solvation shell, as described in more detail in the text.

continuum solvation model). A subsequent second proton transfer together with O_2 generation and water coordination would complete the oxygen-generating step of the catalytic cycle, but the predicted free energy of activation associated with TS structure **b** is much too high to be consistent with experiment and this mechanism additionally fails to be consistent with the isotope labeling experiments described above.

The alternative reaction path 2 in Figure 9 begins with formation of an O−O bond between the two oxo termini. The TS structure **c** has a forming O−O bond length of 1.715 Å and is associated with free energies of activation of 64.9 and 64.0 kJ/mol in the gas phase and aqueous solution, respectively. The resulting μ(1,2) peroxide intermediate **d** is predicted to have a singlet ground state and to be 50.2 kJ/mol higher in energy than **a** in aqueous solution. If we adopt CASPT2 electronic energies in place of M06-L energies for the conversion of **a** to **d**, we predict the relative energies of **c** and **d** in aqueous solution to be 74.8 and 69 kJ/mol, respectively. In the next step on path 2, a water molecule displaces one terminus of the peroxide from a Ru center. The modeling of TS structure **e** requires some care, however. In the gas phase, a TS structure can be found involving a single water molecule displacing one end of the peroxide fragment (Figure 10). The predicted free energy of activation in aqueous solution, relative to **a**·H_2O, is 113.4 kJ/mol. This value may be compared to a prior prediction of Yang and Baik[16] at the B3LYP level of 136.0 kJ/mol. As noted above, on the basis of other benchmark studies we consider the M06-L value to be the more reliable in this instance. However, while the M06-L activation free energy is substantially lower than the previous B3LYP value, it remains somewhat higher than the experimental value, which at 298 K should be 96.6 kJ/mol (cf. data in Table 2).[20]

Closer inspection of the TS structure **e** itself reveals that the incoming water molecule makes a hydrogen bond to the O atom of the peroxide that remains bound to the second Ru atom. This hydrogen bond is stabilizing, but it is not optimal insofar as it

Table 3. Relative Isotopic Ratios of Evolved Molecular Oxygen at the First Turnover Using Different Degrees of Labeled Catalyst and Solvent Together with the Corresponding Calculated Values Assuming Different Reaction Mechanisms

entry	^{18}O (%)[a]		Exch[b]	Nuc[c]	Intra[d]	exptl
1	cat, −	$^{32}O_2$	77.44	88.00	99.52	99.50
2	solv, 12.00	$^{34}O_2$	21.12	12.00	0.48	0.47
3		$^{36}O_2$	1.44	2e-4	4.10^{-4}	0.03
4	cat, 16.13	$^{32}O_2$	77.60	74.60	70.34	69.97
5	solv, 11.90	$^{34}O_2$	21.00	14.50	27.05	27.48
6		$^{36}O_2$	1.40	1.90	2.61	2.55
7	cat, 22.73	$^{32}O_2$	66.39	62.96	59.70	60.20
8	solv, 18.52	$^{34}O_2$	30.18	32.83	35.13	35.10
9		$^{36}O_2$	3.43	4.21	5.17	4.70

[a] This column indicates the degree of catalyst ^{18}O labeling as well as that of the solvent. [b] Exch, exchange, refers to the relative ratios of isotopic O_2 obtained in the case of a fast exchange process with the solvent. [c] Nuc, calculated ratios in the case the mechanism consists of a nucleophilic attack from the solvent to the Ru=O. [d] Intra, calculated ratios in the case the mechanism consists of an intramolecular oxygen−oxygen coupling from the Ru=O groups.

is the departing O atom of the peroxide unit that acquires a proton from water in the subsequent hydroxo/hydroperoxo intermediate **f**. Attempts to adjust the hydrogen bonding in **e** to facilitate such a transfer were unsuccessful as the geometric constraints associated with the making and breaking Ru−O bonds were not compatible with an alternative hydrogen-bonding pattern. However, when a *second* water molecule was introduced in a TS structure **e**·H_2O, it was possible to optimize the hydrogen bonding pattern (see Figure 10) and the free energy of activation, now relative to H_2O + **a**·H_2O (so that reactant **a** is in principle also permitted to enjoy any special benefits associated with microsolvation not accounted for in the continuum solvation model), is reduced to 105.7 kJ/mol in aqueous solution, which is within 9 kJ/mol of the measured value. Including one or more explicit molecules of solvent has been shown to lead to improved agreement with experiment compared to a pure continuum approach in many instances, particularly with respect to the prediction of pK_a values and oxidation−reduction potentials.[18b−d,21] It might be that if we were to include additional explicit water molecules in our model structures that still better agreement with experiment for the activation free energy would be achieved. Unfortunately, the computational demands of such an approach, which include sampling over a possibly large number of low-energy conformations of the microsolvated clusters, prevent us from further evaluating this point.

Because of the very high energy predicted by B3LYP for TS structure **e**, Yang and Baik[16] concluded that mechanistic pathway 2 could not be operative. Instead, they proposed an alternative to pathway 1 involving a protonated form of structure **a**. While they predicted this pathway to have favorable energetics, it is notoriously difficult to predict accurate pK_a values for species like **a**. As the isotope labeling studies are not consistent with a pathway-1-like mechanism, it appears that the free energy cost associated with the protonation equilibrium for **a** was underestimated by the protocol of Yang and Baik. Consideration of structures like **e**·H_2O is not mentioned by Yang and Baik. However, as B3LYP predicts anomalously high energies for TS structure **e**, it is not clear that such modeling would have indicated pathway 2 to be kinetically viable in any case.

The oxygen generation step is completed by displacement of the O_2H unit by another water molecule at the appropriate Ru center with concomitant proton transfer to the hydroxide fragment, thereby generating the reduced form of **a**. This step occurs with a free energy of activation below that of the prior, rate-determining step. Thus, M06-L provides predictions consistent with the observed experimental kinetics and isotope labeling studies, and indicates an important role that water molecules in the first solvation shell may potentially play in stabilizing intermediates or transition-state structures. These observations should prove useful in future modeling studies of water-oxidation catalysts.

2.7. Catalytic Oxygen Generation. In acidic solution containing excess Ce^{IV}, the $H_2O-Ru^{II}Ru^{II}-OH_2$ catalyst generates molecular oxygen very quickly. This process is strongly dependent on the concentration ratios of Ce^{IV} vs Ru catalyst, on the pH, and on the coordinating ability of the acid used. The system $H_2O-Ru^{II}Ru^{II}-OH_2$ 1.0 mM/Ce 100 mM/0.1 M triflic acid with a total volume of 1.38 mL at 25.0 °C gives 24 mM O_2 which indicates a turnover number (TN) of 17.5 and an efficiency of 70% with regard to the Ce^{IV} oxidant. Oxygen evolution profiles vs time are monitored manometrically and graphically represented in Figure 11.

Increasing the ratio of Ox/Cat produces an increase in TN and a decrease in reaction efficiency. For instance, $H_2O-Ru^{II}Ru^{II}-OH_2$ 80 μM/Ce 913 mM/0.1 M triflic acid with a total volume of 1.0 mL at 25.0 °C gives 41 μmols of O_2 which is a TN of 512 and an efficiency of 17.9% with regard to the Ce^{IV} oxidant. The pH effect is also depicted in Figure 11 where the pH is changed from 0.0 to 2.0 while the rest of the parameters remain unchanged. As the figure illustrates, lowering the pH produces an increase in the initial rates of oxygen formation and a slight decrease in TN. Thus, in strongly acidic media the catalyst is faster but it deactivates sooner. The replacement of triflic acid by $HClO_4$ under similar catalytic conditions produces

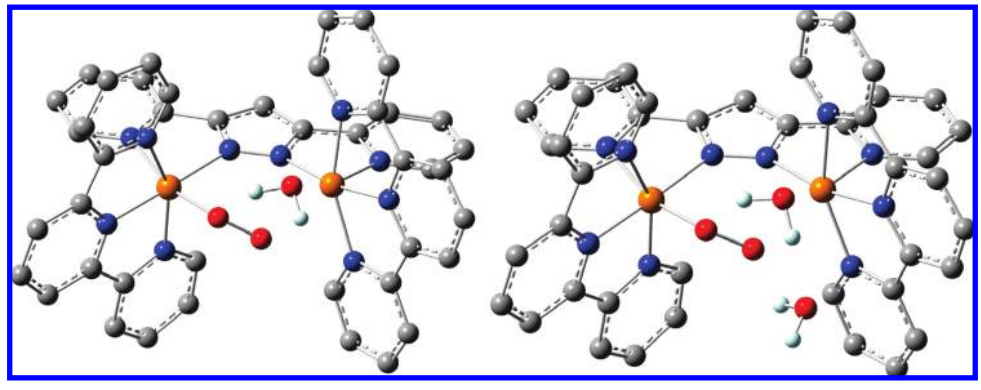

Figure 10. Ball-and-stick representations of **e** (left) and **e**·H_2O (right) at the M06-L level. Ruthenium atoms are maize, oxygen atoms, red; nitrogen atoms, blue; carbon atoms, gray; and hydrogen atoms, white (hydrogen atoms attached to carbon are not shown for clarity).

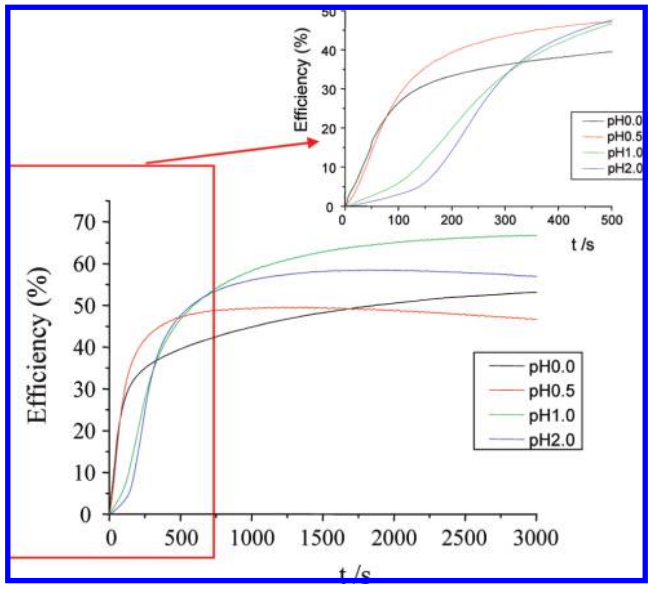

Figure 11. Oxygen evolution vs. time measured by manometry from the reaction of 1.36 μmol of $\mathbf{3}^{3+}$ and 136 μmol of Ce^{IV} in an aqueous CF_3SO_3H solution at pH = 0.0, 0.5, 1.0, and 2.0. Efficiency is defined here as {(mols of O_2)/[(mols of Ce(IV))/4]} × 100.

a slight decrease of TN and also some significant changes in the kinetics of oxygen evolution. This different behavior is attributed to the different coordination capacities of the two anions in species potentially generated by parasitical deactivation pathways off the main catalytic cycle, such as the ones indicated in reactions 25 and 26.

2.8. Potential Deactivation Pathways. We have tried to determine the nature of the species generated after the evolution of molecular oxygen. The addition of excess PF_6^- salt after the addition of 4 equiv of Ce^{IV} produces an orange solid (see the ^{1}H NMR in d_6-acetone in the Supporting Information) that is strikingly similar to that of the initial acetato-bridged complex together with a very small number of other resonances. This clearly suggests that the main structure of the catalyst is maintained after the first turnover. It is also clear that a catalyst capable of oxidizing water to molecular oxygen will be a powerful oxidant for many other organic and inorganic substrates. In this regard, we have observed that performing the experiment in the presence of 0.1 M NaCl generates mainly chlorine gas. Furthermore, slight modifications of the catalyst $\mathbf{3}^{3+}$ drives the reaction to the formation of nearly equal amounts of CO_2 and oxygen,[22] while no CO_2 at all is observed for the case of $\mathbf{3}^{3+}$. Another potential pathway for deactivation is a bimolecular catalyst−catalyst interaction; for instance, a Ru=O group of one catalyst can attack the organic ligand of another catalyst, for example, at the CH group of the pyrazolate moiety. After exhaustive electrochemical oxidation of the $H_2O-Ru^{II}Ru^{II}-OH_2$ complex, we have been able to isolate a very small amount of a dinuclear Ru complex with a ketone group at the relevant position in the pyrazolate moiety. Its crystal structure is shown in the Supporting Information.

3. Discussion

During the past 5 years there have been several complexes of Ru and Ir that were shown to be capable of oxidizing water to molecular oxygen.[23] However, in most cases mechanistic details were lacking and proposed mechanisms were highly speculative in the absence of experimental evidence. Typically the stable molecular entities were catalyst precursors and the real species involved in the catalytic cycles were not known. There are several issues that make mechanistic determinations challenging. One is the intrinsic complexity of the reaction, where the catalyst is likely to cycle among five different oxidation states whether metal- or ligand-based or both.[24] This imposes a requirement for transition metal complexes that are sufficiently long-lived to be able to perform the reaction and also to be spectroscopically detectable. Another intrinsic problem is the unavoidable use of water as solvent, which is problematic due to the limited temperature range at which reactions can be studied, and the high absorptivity of water, which hampers the proper use of techniques such as UV−vis−near-IR, EPR, etc., that could provide otherwise valuable information. One more problem associated with this reaction is the limited solubility of the catalysts or catalyst precursors in water; some are completely insoluble. This leads to inherent difficulties in measuring physical properties at low concentration and in some cases the difficulty of separating the kinetics of the reactions involved with the solubilization kinetics of the starting complex and/or its intermediates. In some instances organic solvents like acetonitrile have been added to permit the reaction to proceed, but this introduces an increase in mechanistic complexity due to the potential coordination of MeCN with the active species. This is a process that has been recently illustrated for related iron complexes[25] and that is summarized in Scheme 2 for a potential Ru complex.

In addition, the high thermodynamic redox potential needed for water oxidation permits the catalyst to oxidize a broad range of organic and inorganic substrates, so the presence of organic solvents can lead to undesired deactivation pathways.[23,30]

3.1. Solubility and Anion Coordination. The influence of the anions in the catalytic process is a recurrent topic in this field that has been previously discussed for the "blue dimer"[6] and other related systems[26] and that also influences our system. Since most of the reactions are carried out with strong acids at pH = 1.0 or even below, the anion can compete for a coordination site with water, or other potential oxygenated ligands such as peroxides or hydroperoxides, at different stages of the catalytic cycle. In our particular case, the relative disposition of the

(19) Roy, N.; Sproules, S.; Weyhermller, T.; Wieghardt, K. *Inorg. Chem.* **2009**, *48*, 3783.
(20) We note that although CASPT2 is useful for computing state-energy splittings in **e** (and these agree well with M06-L predictions), CASPT2 cannot be employed to evaluate the energy of **e** relative to **a** + H_2O, as the orbital active space for **e** differs substantially from those for **a**, **c**, and **d**.
(21) (a) Pliego, J. R.; Riveros, J. M. *J. Phys. Chem. A* **2002**, *106*, 7434. (b) Uudsemaa, M.; Tamm, T. *J. Phys. Chem. A* **2003**, *107*, 9997–10003. (c) da Silva, C. O.; Mennucci, B.; Vreven, T. *J. Phys. Chem. A* **2003**, *107*, 6630–6637. (d) Kelly, C. P.; Cramer, C. J.; Truhlar, D. G. *J. Phys. Chem. A* **2006**, *110*, 2493–2499. (e) Kelly, C. P.; Cramer, C. J.; Truhlar, D. G. *J. Phys. Chem. B* **2006**, *110*, 16066–16081. (f) Bryantsev, V. S.; Diallo, M. S.; Goddard, W. A. *J. Phys. Chem. B* **2008**, *112*, 9709–9719.
(22) Francas, L.; Sala, X.; Benet-Buchholz, J.; Escriche, L.; Llobet, A. *ChemSusChem.* **2009**, *2*, 321.
(23) (a) Tseng, H.-W.; Zong, R.; Muckerman, J. T.; Thummel, R. *Inorg. Chem.* **2008**, *47*, 11763. (b) Xu, Y.; Akermark, T.; Gyollai, V.; Zou, D.; Eriksson, L.; Duan, L.; Zhang, R.; Akermark, B.; Sun, L. *Inorg. Chem.* **2009**, *48*, 2717. (c) Sartorel, A.; Carraro, M.; Scorrano, G.; De Zorzi, R.; Geremia, S.; McDaniel, N. D.; Bernhard, S.; Bonchio, M. *J. Am. Chem. Soc.* **2008**, *130*, 5006. (d) McDaniel, N. D.; Coughlin, F. J.; Tinker, L. L.; Bernhard, S. *J. Am. Chem. Soc.* **2008**, *130*, 210.
(24) Muckerman, J. T.; Polyansky, D. E.; Wada, T.; Tanaka, K.; Fujita, E. *Inorg. Chem.* **2008**, *47*, 1787.
(25) Collins, M. J.; Ray, K.; Que, L. *Inorg. Chem.* **2006**, *45*, 8009.

Scheme 2. Ru−NCMe/Ru−OH_2 Equilibria

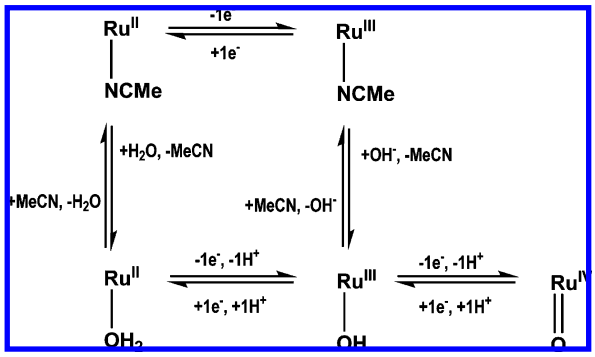

available coordination sites is well suited for a bridging coordination as can be observed in the crystal structures of $\mathbf{2}^{2+}$ and $\mathbf{4}^{2+}$, and such bridging should be even more favorable than in the "blue dimer" case. The coordination of the anion for instance in the acetate case, can take place in two different orientations to generate two enantiomers in the unit cell of the solid-state structure. At room temperature there is a very fast equilibrium between those two enantiomers (activation barrier lower than 19.2 kJ/mol). Even though we do not understand the exact influence of the anion in the catalytic cycle, the anion clearly influences the outcome of our experiments as shown by the different behaviors of the system with 0.1 M triflic or 0.1 M perchloric acid. Furthermore, anion concentration in combination with pH can also influence the process as illustrated in Figure 11, where in the pH range 0.0−0.5 molecular oxygen is generated faster than in the range 1.0−2.0, although the lower pH also leads to more rapid deactivation so that a lower TN is observed for the reaction as a whole.

3.2. Through Space Cooperation and Thermodynamics. It is interesting to note that the first pK_a of the complex $\mathbf{3}^{3+}$ is 6.8 (eq 11); this pK_a is 4 log units lower than that of the corresponding out-mononuclear complex[27] which indicates strong through-space cooperation between the metal centers to generate a $\{Ru_2O_2H_3\}$ entity. This together with the NMR and X-ray data (the latter shows a RuO···ORu distance of 2.50 Å for $\mathbf{3}^{2+}$; the sum of the van der Waals radii for two oxygen atoms is 3.04 Å) suggests that such through-space interactions are important for oxygen atoms in all *in,in* aqua/aqua or aqua/hydroxo complexes. The steric consequences of these interactions will become more manifest when the aqua ligands are substituted by bulkier groups like nitriles, as seen in the substitutions kinetics discussed above and in Table 1.

The Pourbaix diagram for $\mathbf{3}^{3+}$ (Figure 2) indicates four monoelectronic processes to be operative at pH = 1; the first 3 generate a formal oxidation state III,IV and the fourth is chemically irreversible and is associated with the events that ultimately generate molecular oxygen. This is in sharp contrast with the "blue dimer" where the Pourbaix diagram shows one monoelectronic wave assigned to the III,III/III,IV process and a second three-electron wave associated with the III,IV/V,V process.[28] For the $\mathbf{3}^{3+}$ case the four successive 1 e− processes greatly simplify the spectroscopic characterizations of each oxidation state as well as the kinetics associated with the electron transfer reactions that take the initial $Ru^{II}Ru^{II}$ species to the formal $Ru^{IV}Ru^{IV}$ intermediate. We find that the first three ET processes are very fast and the last one, the one that generates the $Ru^{IV}Ru^{IV}$ active species, is slow. Assuming the oxyl radical nature of oxidation states after III,III as suggested by the DFT and CASPT2 studies, the last step, eq 17, could be rewritten as

$$\cdot O-Ru^{III}Ru^{III}-OH_2 + Ce^{IV} \xrightarrow{k_{ET4}} \cdot O-Ru^{III}Ru^{III}-O\cdot + Ce^{III} + 2H^+ \quad (27)$$

The slowness of this process compared to the three previous ET steps could be associated with the need to remove $2H^+$ from the same aqua ligand. Luckily this last ET process has been nicely kinetically characterized because the events that lead to the release of molecular oxygen are substantially slower than the preceding ET reactions. This is again in sharp contrast with the "blue dimer" where the slowest step is associated with an ET process[6c] although other studies in acidic media suggest that the decay from $Ru^{V}Ru^{V}$ oxidized state is rate limiting.[6b]

3.3. O−O Bond Formation Mechanisms. The kinetics, oxygen labeling experiments, and DFT and CASPT2 modeling all indicate a mechanism where the oxygen−oxygen bond formation event is intramolecular. Potential mechanisms involving rapid formation of hydrogen-bonded dimers in solution that could undergo bimolecular oxygen evolution so as to generate the same isotopic distributions are discarded based on the DOSY experiments that indicate that such species are not formed. Moreover there is no precedent in the literature for this type of phenomena with typical Ru−OH_2 complexes.[29] Calculations predict the formation of a μ(1,2)-peroxo bridged di-Ru(III) complex, **d** (see Figure 9), that evolves to a terminal hydroperoxo, **f**, and finally releases molecular oxygen and generates the initial catalyst in its lower oxidation state. Those two processes are the slowest processes for the system and thus constitute the rate determining steps. Careful analysis of these two processes indicates that in our system these slow processes are associated in part with a spin mismatch for the oxyl−oxyl coupling to form species **d** (the ground electronic state of **a** is a quintet while **c** and **d** are singlets) and peroxo ligand substitution/proton management for the second process to form species **f**. The latter point is particularly interesting because the possible exit pathways, as well as the energetics, associated with proton management in water oxidation by the Mn-cluster in the OEC-PSII are currently the subject of considerable scrutiny.[30]

The results found here are quite different from those observed for the ^{18}O labeled "blue dimer" where the intramolecular pathway plays a minor role and the dominant Ru-based pathway seems to be water nucleophilic addition. Of course, the structure and electronic properties of the $H_2O-Ru^{II}Ru^{II}-OH_2$ catalyst are radically different from those of the "blue dimer" as has been noted before.[10] In addition, for the $H_2O-Ru^{II}Ru^{II}-OH_2$ case the bridging ligand is rigid and the molecule is designed in such a way that the two Ru−OH_2 are oriented cis to one another and interacting through space. Thus when species **a** is formed the oxygen atoms are properly oriented so that no additional and energetically costly bond/angle deformations are required to bring the two O atoms sufficiently close to effect

(26) Ottenwaelder, X.; Rudd, D. J.; Corbett, M. C.; Hodgson, K. O.; Hedman, B.; Stack, T. D. P. *J. Am. Chem. Soc.* **2006**, *128*, 9268.
(27) Sens, C.; Rodríguez, M.; Romero, I.; Llobet, A.; Parella, T.; Benet-Buchholz, J. *Inorg. Chem.* **2003**, *42*, 8385.
(28) Gilbert, J. A.; Eggleston, D. S.; Murphy, W. R., Jr.; Geselowitz, D. A.; Gestern, S. W.; Hodgson, D. J.; Meyer, T. J. *J. Am. Chem. Soc.* **1985**, *107*, 3855.
(29) Meyer, T. J.; Huynh, M. H. V. *Inorg. Chem.* **2003**, *42*, 8140.
(30) (a) Murray, J. W.; Barber, J. *J. Struct. Biol.* **2007**, *159*, 228. (b) Ishikita, H.; Saenger, W.; Loll, B.; Biesiadka, J.; Knapp, E.-W. *Biochemistry* **2006**, *45*, 2063.

O−O bond formation; the ligand topology also provides a favorable entropic situation for the occurrence of an intramolecular event,[31] although there may also be entropic effects associated with the surrounding aqueous solvent shell that we have not considered.

4. Conclusions

We have presented a comprehensive study of the $H_2O-Ru^{II}Ru^{II}-OH_2$ complex employing electrochemical, spectroscopic, kinetic, and theoretical techniques. The complexity of the system requires the application of all of these techniques in order to characterize the reaction mechanism responsible for oxygen−oxygen bond formation. The catalyst shows a complex and delicate balance of reactions. Future water-oxidation catalyst design efforts will need to address several critical factors including the nature of the transition metal, oxidation states available to the transition metal, the nuclearity of the complex, electronic couplings between multiple metal centers, the stability of supporting ligands, the nucleating ability of ligands, the geometrical disposition of the ligand(s), and the active versus auxiliary role of the ligands. To better characterize reaction intermediates having higher oxidation states, we are combining new spectroscopic studies (EPR, XAS, rR) with a more detailed analysis of our multireference wave functions, and we will report these results in due course.

Acknowledgment. Support was received from SOLAR-H2 (EU 212508), ACS (PRF 46819-AC3) and the MICINN (Consolider Ingenio 2010 (CSD2006-0003), CTQ2007-67918, and CTQ2007-60476). C.J.C. and L.G. thank the U.S. and Swiss National Science Foundations, respectively (Grants CHE-0610183 and 200021-111645/1). Nora Planas of ICIQ is gratefully acknowledged for some drawings and NMR experiments.

Supporting Information Available: Experimental Section together with spectroscopic, crystallographic, and kinetic data and results of calculations. This material is available free of charge via the Internet at http://pubs.acs.org.

JA9036127

(31) Evidence for this type of mechanism has also been found for the case of the dinitrogen formation using a related oxo-bridged dimer. See: Ishitani, O.; Ando, E.; Meyer, T. *J. Inorg. Chem.* **2003**, *42*, 1707.